New genus of extinct Holocene gibbon associated with humans in Imperial China

Summary: We describe a new globally extinct genus and species of gibbon from a late Holocene royal tomb in China, representing the first documented primate extinction from a postglacial continental ecosystem, and suggesting that until recently eastern Asia supported a previously unknown, historically extinct endemic radiation of apes.

Authors: Samuel T. Turvey[1,*], Kristoffer Bruun[2], Alejandra Ortiz[3], James Hansford[1,4], Songmei Hu[5], Yan Ding[5], Tianen Zhang[5], Helen J. Chatterjee[2]

[1]Institute of Zoology, Zoological Society of London, Regent's Park, London NW1 4RY, UK. [2]Department of Genetics, Evolution & Environment, University College London, Gower Street, London WC1E 6BT, UK. [3]Institute of Human Origins, School of Human Evolution and Social Change, Arizona State University, Tempe, AZ 85281, USA. [4]Ocean and Earth Science, National Oceanography Centre Southampton, University of Southampton Waterfront Campus, Southampton, UK. [5]Shaanxi Provincial Institute of Archaeology, Xi'an 710054, China.

To whom correspondence should be addressed. Email: samuel.turvey@ioz.ac.uk

Although all extant apes are threatened with extinction, there is no evidence for human-caused extinctions of apes or other primates in postglacial continental ecosystems, despite intensive anthropogenic pressures associated with biodiversity loss for millennia in many regions. Here we report a new, globally extinct genus and species of gibbon, *Junzi imperialis*, described from a partial cranium and mandible from a ~2,200-2,300 year-old tomb from Shaanxi, China. *Junzi* can be differentiated from extant hylobatid genera and the extinct Quaternary gibbon *Bunopithecus* using univariate and multivariate analyses of craniodental morphometric data. Primates are poorly represented in the Chinese Quaternary fossil record, but historical accounts suggest that China may have contained an endemic ape radiation that has only recently disappeared.

A Warring States period tomb excavated in 2004 at Shenheyuan, Xi'an (formerly the ancient capital Chang'an), Shaanxi, possibly attributable to Lady Xia, grandmother of China's first emperor Qin Shihuang (259-210 BC), contains 12 pits with animal remains (Fig. 1) (*1, 2*). Similar tomb menageries are known from other Chinese high-status burials of comparable age (*3*). Pit K12 contains skeletons of leopard (*Panthera pardus*), lynx (*Lynx lynx*), Asiatic black bear (*Ursus thibetanus*), crane (*Grus* sp.), domestic mammals and birds (*1*), and a gibbon (Shaanxi Provincial Institute of Archaeology, Shenheyuan M1K12:3).

Gibbons and siamangs (Hylobatidae) include four living genera (*Hoolock*, *Hylobates*, *Nomascus*, *Symphalangus*) containing 20 species (*4, 5*). Six extant species are known historically from China (*5, 6*). Gibbons were considered culturally significant throughout Chinese history; their perceived "noble" characteristics made them symbols of scholar-officials (*junzi*), and they became

high-status pets from the Zhou Dynasty (1046-256 BC) (*7*). They are extremely scarce in China's Pleistocene-Holocene record, and most pre-modern remains are isolated teeth or postcrania insufficiently diagnostic for species-level or genus-level identification (*8, 9*). The most complete Quaternary Chinese hylobatid is a left mandibular fragment from Chongqing (AMNH-18534), probably early-middle Pleistocene in age, described in 1923 as an extinct genus and species, *Bunopithecus sericus* (*10*). In contrast, M1K12:3 includes a partial facial skeleton (missing the posterior neurocranium) with complete anterior dentition, left-right PM3-4 and right M1-2; an associated right M3; a partial mandible with almost complete anterior dentition (missing left I2), left-right pm3-4 and right m1-2; and non-diagnostic right distal forelimb elements (Fig. 1).

Destructive sampling of M1K12:3 was not possible due to the unique specimen's protected archaeological status, and previous attempts to amplify DNA from Chinese Holocene samples have often proved unsuccessful due to poor biomolecule preservation under subtropical conditions (*11*), so we conducted multivariate and univariate morphometric analyses to determine its affinities to other hylobatids. First, we conducted canonical variate analyses (CVA) using 16 cranial landmarks shared between M1K12:3 and a dataset including all extant hylobatid genera (*Hoolock*, n=53; *Hylobates*, n=327; *Nomascus*, n=34; *Symphalangus*, n=63) (*12*, *13*). We partially restored a three-dimensional scan of the M1K12:3 cranium before analysis, through mirror-imaging and reference-based reconstruction of the zygomatic bone, zygomatic arch, posterior maxilla and posterior frontal (*13*). Landmarks are distributed across nearly the entire remaining or restored cranial surface. All CVAs were performed using genus as classifying variable when assessing the position of M1K12:3 in morphospace.

Permutation tests (10,000 rounds) for between-group Procrustes and Mahalanobis distances show significant differentiation between all extant genera (p<0.0001, all comparisons), and between M1K12:3 and extant genera (Fig. 2, Table 1, Table S1). CV1 (60.90% variation) is associated with expansion of the facial region and primarily separates *Symphalangus*, the largest, most morphologically distinct hylobatid. CV2 (23.04% variation) represents shape changes to the frontal, orbit and infraorbital region, and strongly differentiates M1K12:3 from extant genera due to its expanded upper anterior neurocranium: M1K12:3 exhibits a more superior position of the frontal posterior margin (bregma, stephanion), the anterior margin (glabella, upper orbital rim) has undergone an inferior shift, the zygomaxillary suture is shortened to give a narrower cheekbone, and molar dentition is more widely set together with an inferior shift (Table S2). Posterior probabilities indicate extremely high classification accuracy (96-97%; Table S3), with M1K12:3 consistently classified as a separate group.

We collected molar (M1-3, m1-2) landmark data (homologous landmarks at main cusp tips, 20 (upper) or 22 (lower) semi-landmarks along outline), tooth crown areas (maximum occlusal area), polygon areas (ratio from lines connecting cusps relative to total occlusal area), and cusp angles (calculated from homologous landmark coordinates) from M1K12:3 (*13*). We compared these data with a new dataset containing morphometric data for 789 hylobatid molars representing 279 individuals (*Hoolock*, n=77; *Hylobates*, n=129; *Nomascus*, n=41; *Symphalangus*, n=32), including all extant Chinese species and AMNH-18534 (*13*).

Permutation tests (10,000 rounds) for Mahalanobis distances again show significant differentiation between all extant genera (p<0.001, all comparisons), although Procrustes distances do not consistently differentiate extant genera, especially *Nomascus* (Table S5). M1K12:3 is statistically differentiated from extant genera in several features including occlusal area (significantly larger M2, M3 and m2 than *Hylobates*; significantly smaller M1, m1 and m2 than *Symphalangus*), larger M3 paracone angle than *Nomascus*, and smaller protoconid, metaconid, entoconid and/or hypoconid angles than all genera (Fig. S4, Tables S6-S7). CVAs derived from semi-landmark data demonstrate the distinctive molar shape of M1K12:3. M3, m1 and m2 all fall outside the range of extant hylobatid variation (Fig. 2), and have high CVA classification accuracy (76-86%; Table S3). Permutation tests for Procrustes and Mahalanobis distances show significant differentiation between M1K12:3 and extant hylobatids for upper and/or lower molar outline; pairwise distances are greater than between extant genera (Table 1, Table S1). CVA for m2, the only tooth shared by M1K12:3 and AMNH-18534, demonstrates these specimens are also morphologically distinct (Fig. 2); *Bunopithecus* shows a very different relationship to extant hylobatids compared to M1K12:3, with a likely close relationship to *Hoolock* (*10*).

While these analyses cannot reconstruct M1K12:3's phylogenetic affinities, even genomic analyses have proved unable to clarify higher-order hylobatid relationships, possibly because living genera diverged through near-instantaneous radiation ~5 million years ago (*14*). However, cranial and molar data clearly differentiate M1K12:3 from living hylobatids and the only other Chinese Quaternary hylobatid. We therefore describe M1K12:3 as a new extinct

121 genus and species, *Junzi imperialis* (*15*). Although other Holocene primate losses
122 are known (21 extinctions in "ecologically naïve" Madagascan and Caribbean
123 island faunas, with two species persisting beyond 1500 AD; *16, 17*), the
124 disappearance of *J. imperialis* constitutes the first documented postglacial
125 extinction of an ape, or of any continental primate.

126 Gibbons are today restricted to southwestern China (*6*), with closest
127 populations >1,200km from Chang'an and separated by major drainages (Fig. 1).
128 Large rivers can represent barriers to gene flow in hylobatids (*18*), providing
129 biogeographic support for evolutionary differentiation of central Chinese
130 gibbons. Chang'an was an important regional power centre under the Qin State
131 and became China's political and economic centre during the Han Dynasty (*19*);
132 gibbons could therefore have been transported to Chang'an as trade items or
133 tributes. However, other mammals from the Shenheyuan tomb still occur in
134 Shaanxi (*6*), suggesting a similar local origin for M1K12:3. Contemporary
135 accounts describe gibbons being caught near Chang'an into the 10th century (*7*),
136 and gibbon survival in Shaanxi until the 18th century (*20*). Southern Shaanxi
137 represents the northern limit of China's subtropical forest ecoregion, and retains
138 remnant populations of primates and other mammals (e.g. giant pandas) that co-
139 occurred with gibbons in Quaternary assemblages (*6, 21*).

140 Global ecosystems have experienced extreme human-caused biodiversity
141 loss in recent centuries, with extinction rates elevated by several orders of
142 magnitude; it is increasingly accepted that a mass extinction is underway (*22,*
143 *23*). Eastern and southeast Asian biotas have been disrupted disproportionately:
144 this region contains the most threatened mammals (*4*), and 73% of Asian
145 primates are threatened compared to 60% globally (*24*). In China, two gibbon

146 species (*Hylobates lar*, *Nomascus leucogenys*) have recently disappeared,
147 surviving species are all critically endangered, and the Hainan gibbon (*Nomascus*
148 *hainanus*) may be the world's rarest mammal with ~26 surviving individuals (*4*).
149 The background mammalian extinction rate is estimated at 1.8
150 extinctions/million species/year (*22*). As 525 Holocene-Recent primates,
151 including 27 apes, are recognized (*5, 24, 25*), expected background extinction
152 rates are 9.45×10^{-4}/year for primates, and 4.86×10^{-5}/year for apes. We could
153 therefore expect 11.1 background primate extinctions and 57% probability of
154 background ape extinction across the 11,700-year Holocene (although only 45%
155 probability of primate extinction and 2% probability of ape extinction since 1500
156 AD, the IUCN threshold used to assess human-caused extinctions (*4*), and the
157 period into which *J. imperialis* likely persisted). A hypothesis of "natural" rather
158 than anthropogenically-mediated extinction of *J. imperialis* therefore cannot be
159 discarded completely. However, few extinctions across the climatically stable
160 Holocene can even questionably be interpreted as non-anthropogenic (*16*).
161 Central Chinese landscapes have supported amongst the world's highest human
162 densities for millennia (*19*), and experienced extensive Holocene mammal
163 extinctions (*21*). The discovery of M1K12:3 in a tomb provides direct evidence of
164 human exploitation, and extensive deforestation occurred near Chang'an during
165 the late Imperial period, with remaining high-elevation forests representing
166 suboptimal gibbon habitat (*26*). Analysis of predictors of Chinese Holocene
167 mammal range loss has shown that best-supported models include an index of
168 anthropogenic impact (*21*), and reconstruction of historical gibbon decline
169 across China demonstrates extinction following a wavefront of directional
170 pressures that matches known human population expansion (*20*).

Although primates are disproportionately threatened today (*24*), previous studies suggest they have not experienced elevated levels of past extinction (*27*). However, they are under-represented in Quaternary archives, which remain understudied across most areas of primate distribution (*8*, *21*). Our description of *J. imperialis* suggests past human-caused primate diversity loss may be underestimated, with important implications for understanding extinction vulnerability and informing conservation (*24*). Our findings also emphasize the extreme vulnerability of hylobatids even compared to other primates. Historical records document former gibbon occurrence across central and southern China (*7, 20*), in areas separated from distributions of extant species and *J. imperialis* by major drainages (Fig. 1). These populations may represent undescribed extinct species, suggesting much greater historical loss of global ape diversity. We encourage further investigation of Asian environmental archives to reconstruct past human-caused biodiversity loss in this global conservation hotspot, and provide new insights for understanding faunal vulnerability and resilience to help prevent future extinctions.

References and Notes

1. T. Zhang, N. Hou, Y. Ding, Shaanxi Chang'an faxian Zhanguo Qinlingyuan yizhi [Discovery of a Warring States period tomb of the Qin State, Chang'an, Shaanxi]. *Zhongguo Wenwubao* ***2006***, 1-2 (2006).
2. Y. Ding, Shenheyuan Zhanguo Qinlingyuan zhuren shitan [Identifying the owner of the Shenheyuan Warring States period tomb of the Qin State]. *Kaogu Yu Wenwu* ***2009***, 62-66 (2009).

3. X. Wang, Han Nanling daxiongmao he xiniu tanyuan [Study on giant panda and rhinoceros from the "southern tomb" of the Han Dynasty]. *Kaogu Yu Wenwu* ***1983***, 89-91 (1983).
4. IUCN, *The Red List of Threatened Species. Version 2017-2* (2017).
5. P. Fan *et al*., Description of a new species of *Hoolock* gibbon (Primates: Hylobatidae) based on integrative taxonomy. *Am. J. Primatol.* ***79***, e22631 (2017).
6. A. T. Smith, Y. Xie (Eds.), *A Guide to the Mammals of China* (Princeton University Press, Princeton, NJ, 2008).
7. R. H. Van Gulik, *The Gibbon in China: An Essay in Animal Lore* (E. J. Brill, Leiden, 1967).
8. N. G. Jablonski, G. Chaplin, "The fossil record of gibbons" in *The Gibbons: New Perspectives on Small Ape Socioecology and Population Biology*, D. Whittaker, S. Lappan, Eds. (Springer, Dordrecht, 2009), pp. 110-130.
9. Y. Gu, Preliminary research on the fossil gibbons of the Chinese Pleistocene and recent. *Hum. Evol*. ***4***, 509-514 (1989).
10. A. Ortiz *et al*., The taxonomic and phylogenetic affinities of *Bunopithecus sericus*, a fossil hylobatid from the Pleistocene of China. *PLoS ONE* ***10***, e0131206.
11. S. T. Turvey *et al*., Holocene range collapse of giant muntjacs and pseudo-endemism in the Annamite large mammal fauna. *J. Biogeogr.* ***43***, 2250-2260 (2016).
12. N. Creel, H. Preuschoft, "Cranial morphology of the lesser apes" in *Gibbon and Siamang, Vol. 4*, D. M. Rumbaugh, Ed. (Karger, Basel, 1976), pp. 219-303.
13. Materials and methods are available online as supporting online material.

14. L. Carbone *et al*., Gibbon genome and the fast karyotype evolution of small apes. *Nature* ***513***, 195-201 (2014).
15. Systematic paleontology is available online as supporting online material.
16. S. T. Turvey, *Holocene Extinctions* (Oxford University Press, Oxford, 2009).
17. S. B. Cooke, A. L. Rosenberger S. T. Turvey, An extinct monkey from Haiti and the origins of the Greater Antillean primates. *Proc. Natl Acad. Sci. USA* 108: 2699-2704 (2011).
18. V. N. Thinh *et al*., Mitochondrial evidence for multiple radiations in the evolutionary history of small apes. *BMC Evol. Biol*. ***10***, 74 (2010).
19. L. Liu, X. Chen, *The Archaeology of China: From the Late Paleolithic to the Early Bronze Age* (Cambridge University Press, Cambridge, 2012).
20. S. T. Turvey, J. J. Crees, M. M. I. Di Fonzo, Historical data as a baseline for conservation: reconstructing long-term faunal extinction dynamics in Late Imperial-modern China. *Proc. Roy. Soc. B* ***282***, 20151299 (2015).
21. S. T. Turvey, J. J. Crees, Z. Li, J. Bielby, J. Yuan, Long-term archives reveal shifting extinction selectivity in China's postglacial mammal fauna. *Proc. Roy. Soc. B* ***284***, 20171979 (2017).
22. A. D. Barnosky *et al*., Has the Earth's sixth mass extinction already arrived? *Nature* ***471***, 51-57 (2011).
23. G. Ceballos *et al*., Accelerated modern human-induced species losses: entering the sixth mass extinction. *Sci. Adv.* ***1***, e1400253 (2015).
24. A. Estrada *et al*., Impending extinction crisis of the world's primates: why primates matter. *Sci. Adv.* ***3***, e1600946 (2017).
25. A. Nater *et al*., Morphometric, behavioral, and genomic evidence for a new orangutan species. *Curr. Biol.* ***27***, 1-12 (2017).

26. R. B. Marks, *China: An Environmental History* (Rowman & Littlefield, Lanham, MD, 2017).
27. S. T. Turvey, S. A. Fritz, The ghosts of mammals past: biological and geographical patterns of global mammalian extinction across the Holocene. *Phil. Trans. Roy. Soc. B* ***366***, 2564-2576 (2011).
28. S. Benazzi, G. Gruppioni, D. S. Strait, J. J. Hublin, Technical note: virtual reconstruction of KNM-ER 1813 *Homo habilis* cranium. *Am. J. Phys. Anthropol.* ***153***, 154-160 (2014).
29. P. Gunz, *Statistical and Geometric Reconstruction of Hominid Crania: Reconstructing Australopithecine Ontogeny* (PhD dissertation, University of Vienna, 2005).
30. D. C. Adams, F. J. Rohlf, D. E. Slice, Geometric morphometrics: ten years of progress following the 'revolution'. *Italian J. Zool.* ***71***, 5-16 (2004).
31. D. F. Wiley, *Landmark Editor 3.0* (IDAV, University of California, Davis, 2006). Available at <http://graphics.idav.ucdavis.edu/research/Evo-Morph>
32. C. P. Klingenberg, MorphoJ: an integrated software package for geometric morphometrics. *Molec. Ecol. Res.* ***11***, 353-357 (2011).
33. S. E. Bailey, *Neandertal Dental Morphology: Implications For Modern Human Origins* (PhD dissertation, Arizona State University, 2002).
34. V. C. Pilbrow, *Dental Variation in African Apes with Implications For Understanding Patterns of Variation in Species of Fossil Apes* (PhD dissertation, New York University, 2003).
35. A. Ortiz, *The Influence of Development and Homology on Hominin Molar Morphological Diversity* (PhD dissertation, New York University, 2016).

36. F. J. Rohlf, *Tps Software* (Ecology and Evolution, SUNY at Stony Brook, 2004). Available at <http://life.bio.sunysb.edu/morphS>
37. S. Molnar, Human tooth wear, tooth function and cultural variability. *Am. J. Phys. Anthropol.* ***34***, 27-42 (1971).
38. Ø. Hammer, D. A. T. Harper, P. D. Ryan, PAST: paleontological statistics software package for education and data analysis. *Palaeontol. Electronica* ***4***, 1-9 (2001).
39. A. H. Schultz, Age changes, variability and generic differences in body proportions of Recent hominoids. *Folia Primat.* ***19***, 338-359 (1973).
40. J. Fleagle, *Primate Adaptation and Evolution* (Academic Press, Amsterdam and Boston, 2013).
41. S. Ye, F. Heule, An evaluation of Robert van Gulik's *The Gibbon in China* and its place in modern Sinological discourse. *Southeast Rev. Asian Stud.* ***35***, 141-160 (2013).
42. D. A. Hooijer, Quaternary gibbons from the Malay Archipelago. *Zool. Verhand. Leiden* ***46***, 1-42 (1960).
43. D. R. Swindler, *Primate Dentition: An Introduction to the Teeth of Non-Human Primates* (Cambridge University Press, Cambridge, 2002).
44. Y. Zhang, A. Ortiz, K. He, T. Harrison, Fossil gibbons (Mammalia, Hylobatidae) from the Pleistocene of Chongzuo, Guangxi Zhuang Autonomous Region, China. *Vertebrat. PalAsiatic.* (in press).

Acknowledgments: Access to collections was provided by: Institute of Zoology, Beijing; Kunming Institute of Zoology; South China Institute of Endangered Animals; Natural History Museum, London; American Museum of Natural

History; Center for the Study of Human Origins; National Museum of Natural History; Museum of Comparative Zoology; Zoological Museum, Vietnam National University. We thank Jessica Korsgaard, Clare Kimock, Heidi Ma and Ben Garrod for assistance.

Funding: Research was supported by a Royal Society University Research Fellowship (UF080320/130573).

Author contributions: S.T.T. and H.J.C. designed research; J.H., A.O., S.H., Y.D., T.Z., S.T.T. and K.B. collected data; K.B., A.O. and H.J.C. analysed data; S.T.T., A.O. and H.J.C. wrote the paper.

Competing interests: None declared.

Data and materials availability: All data needed to evaluate the conclusions in the paper are present in the paper or the Supplementary Materials.

Supporting Online Material

Fig. 1. Cranium and mandible of *Junzi imperialis* holotype (M1K12:3): **A**, cranium, anterior view; **B**, mandible, lateral view; **C**, upper dentition, occlusal view; **D**, lower dentition, occlusal view; **E**, right M3. Scale bar=10mm. Inset, Modern distribution of hylobatids (dark grey; modified from ref. 18) and historical distribution across China (pale grey; modified from ref. 20), showing Chang'an (star), *Bunopithecus sericus* collection locality (filled circle), and major rivers.

Fig. 2. Plots of first two canonical variates (CV1-2) of hylobatid cranial and molar analyses. M1K12:3, red; *Bunopithecus*, black (m2 only); *Hoolock*, green; *Hylobates*, orange; *Nomascus*, purple; *Symphalangus*, blue. Cranial plot includes both reconstructions of M1K12:3.

Table 1. Comparisons between M1K12:3 and extant hylobatids for permutation tests (10,000 rounds) of cranial and molar Procrustes and Mahalanobis distances (bold, significant difference).

Extant hylobatid genus	**Procrustes distance**						**Mahalanobis distance**					
	Cranium	M1	M2	M3	m1	m2	Cranium	M1	M2	M3	m1	m2
Hoolock	**>0.001**	0.164	0.116	0.117	0.222	0.092	**>0.001**	0.099	0.075	**0.030**	**0.005**	**0.006**
Hylobates	**>0.0001**	0.345	0.165	0.191	0.053	**0.035**	**>0.0001**	0.161	0.128	**0.034**	**0.010**	**0.003**
Nomascus	**0.001**	0.437	0.263	0.152	0.399	0.141	**>0.001**	0.296	0.401	0.062	**0.018**	**0.042**
Symphalangus	**>0.001**	**0.030**	0.065	0.054	0.823	0.343	**>0.001**	0.126	**>0.001**	0.052	0.088	**0.004**

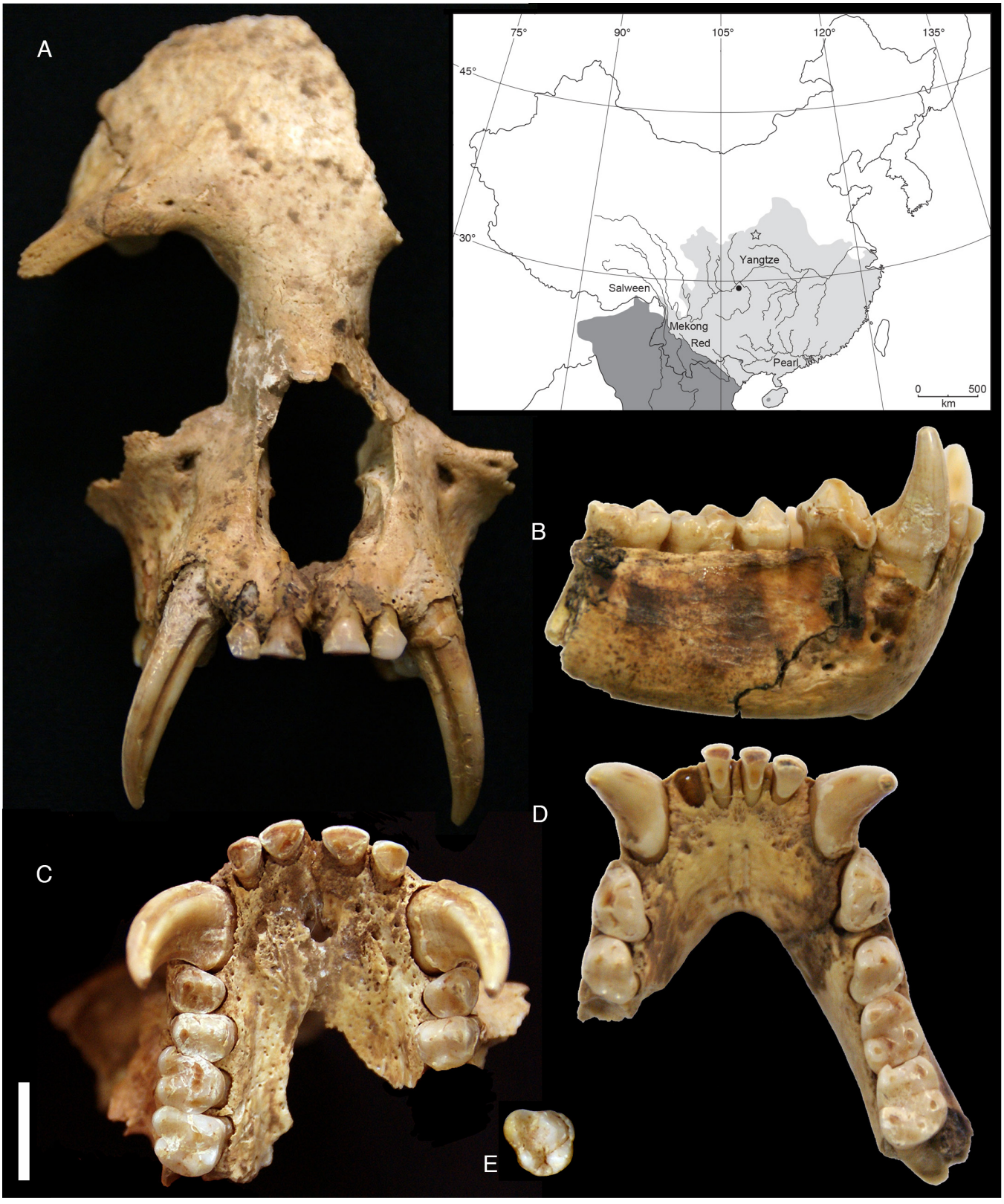
A
75°
90°
105°
120°
135°
45°
30°
Yangtze
Salween
Mekong
Red
Pearl
0
500
km
B
C
D
E

Cranium

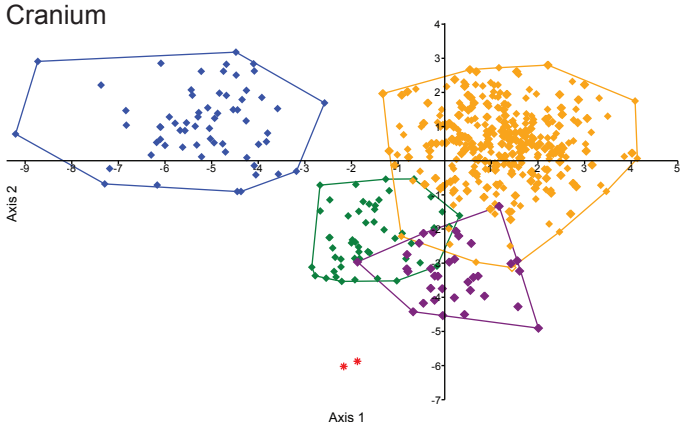

M1

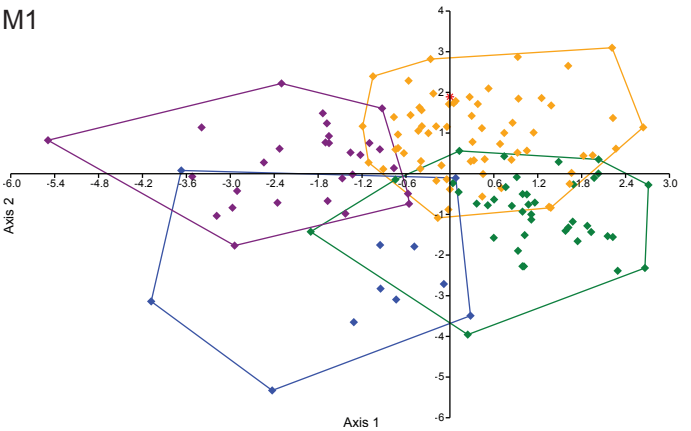

M2

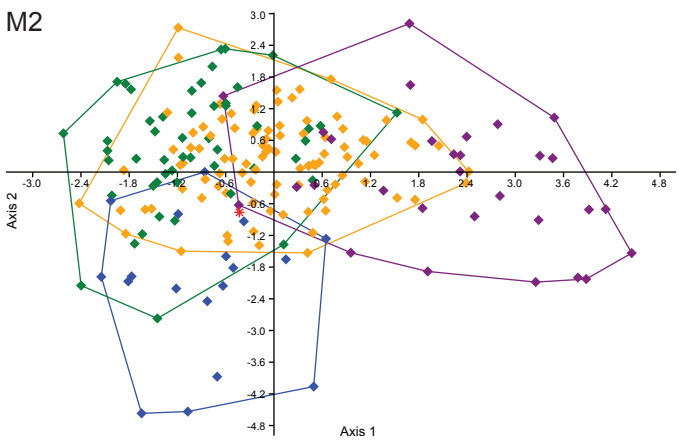

M3

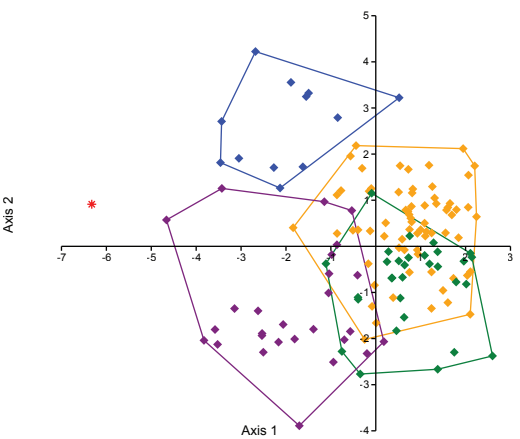

m1

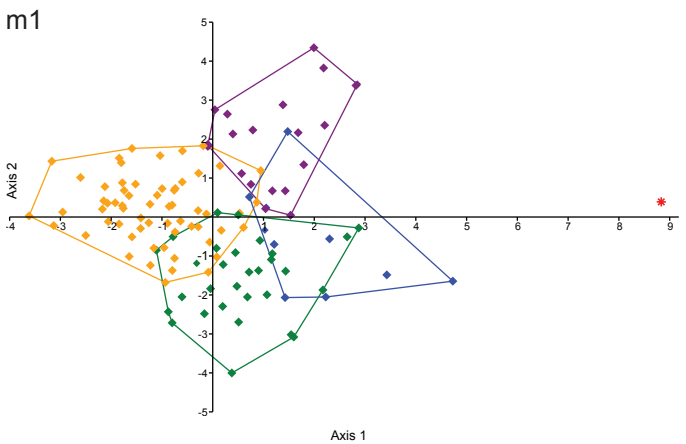

m2

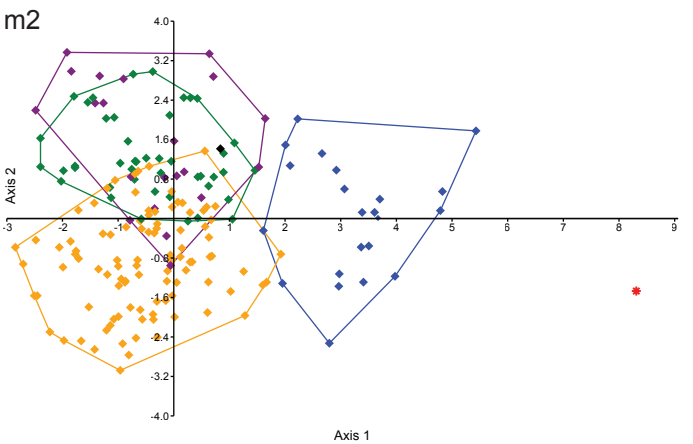

Supporting Online Material: Materials and methods

1. ZOOARCHAEOLOGICAL DATA COLLECTION

The fragile facial skeleton and mandible of M1K12:3 were scanned at the Shaanxi Provincial Institute of Archaeology using a NextEngine 3D Laser Scanner to capture the entire available surface morphology. ScanStudioHD software (NextEngine, 2006) was used to operate the scanner; we utilized the software's scan-editing features to volume-merge two separate 360° scans that captured the specimen in different orientations, to incorporate as much surface morphology as possible for analysis. This merged three-dimensional scan was used for all subsequent cranial, mandibular, and molar morphometric analyses.

2. CRANIAL DATA

Reconstructing M1K12:3

The most superior section of the maxilla of M1K12:3, which forms the narrowest region connecting orbital rim to nasal aperture, is damaged on the right side and has previously been repaired with plaster material. There is also some evidence of taphonomic distortion of the cranium: the right dentition is located slightly more anterior to the left dentition in what appears to be an unnatural degree of asymmetry, which is probably partly caused by the fact that the medial palatine suture is obliterated and the resultant gap between both sides of the palate has been filled with plaster material. There may also be further left/right displacement effects on anatomy located further superior to the palate region. To address this distortion, we only used the

better-preserved right side for shape analyses to avoid the confounding effects of this bilateral asymmetry on results. We removed the plastered area on the upper right maxilla from the three-dimensional scan using Avizo 9.0 (Visualisation Sciences Group, Inc.) and mirror-imaged the preserved area from the left side across the midsagittal plane to restore the upper right maxilla. We also mirror-imaged the better-preserved lower margin of the left orbital rim to restore lost morphology on the right side.

Areas not possible to be restored by mirror-imaging can be estimated through reference-based reconstruction techniques, in which a specifically selected complete reference specimen that is morphologically similar to the target specimen is used to predict missing areas by a thin-plate spline interpolation. The accuracy of such reconstruction depends on the morphological distance between the attempted reconstruction and preserved morphology. Almost all of the neurocranium is missing in M1K12:3, and so any attempt to reconstruct this region when only facial morphology remains would be too extreme to be successful; the extent of an accurate reference-based reconstruction in M1K12:3 is therefore limited to estimating the zygomatic bone, zygomatic arch, posterior maxilla (with M3), and posterior frontal bone. We made three-dimensional scans of two reference crania using the methods described above (*Nomascus concolor*: NHM 33.4.1.2; *Hylobates lar*: NHM 55.1499). These taxa were chosen because M1K12:3 appears relatively similar to *Nomascus* in some facial characteristics (sharing the weakly protruding browridge and high, steep anterior frontal bone characteristic of *Nomascus* relative to other gibbons), and because the high degree of overall morphological similarity between extant gibbons permits selection of references from >1 genus to investigate the extent of morphological variation in producible reconstructions.

We followed the reference-based reconstruction protocol developed by ref. 28. On both reference specimen scans, the midsagittal plane was computed and the entire left hemicranium was removed, and areas on the right hemicranium not selected for reconstruction (the entire neurocranium other than the frontal bone) were selected for removal, to leave only areas congruent with the preserved morphology of M1K12:3 and areas targeted for reconstruction. On the resultant surfaces, we digitized a template for each reference formed of 11 landmarks (bregma, canine fossa, foramen infraorbitale, frontotemporale, glabella, jugale, nasale, nasospinale, orbitale, prosthion, rhinion), 129 curve semi-landmarks (alveolar margin, n=20; anterior nasal aperture, n=9; frontotemporal-zygomatic, n=14; lower zygomatic arch, n=21; midsagittal external, n=25; orbital rim, n=20; upper zygomatic arch, n=20), and 300 surface semi-landmarks, using Viewbox software (dHAL Software, Kifissia, Greece) to map the remaining geometry on the cranial surface; we then used this template to digitize M1K12:3 (the target) with a similar landmark and semi-landmark configuration.

While landmarks remained fixed, we allowed semi-landmarks in both the reference and target specimens to slide along curves (1 degree of freedom, DoF) and surfaces (2 DoF) in order to minimise the bending energy of the thin-plate spline computed between reference and target. Landmarks and semi-landmarks occurring in missing areas of the target specimen (i.e. posterior frontal bone, posterior maxilla, zygomatic bone, zygomatic arch) were declared 'free' and could move without constraints (3 DoF). We then projected the sliding semi-landmarks back onto their respective curves and surfaces. We repeated this spline relaxation and projection process up to a maximum of five times until obtaining a minimum bending energy value, at which point it was necessary to determine by visual inspection whether designating a semi-landmark as "missing" or "present" was correct anatomically, as semi-landmarks that occur around

the edges of preserved morphology may fall into either category after sliding. We reclassified any semi-landmarks that did not fit their original designation and repeated the above sliding process with this adapted semi-landmark coding, repeating this process as many times as was necessary to optimise the distribution of semi-landmarks. Following this repeated process, all points between reference template and target specimen can be considered geometrically corresponding (*29*). We interpolated using the TPS function to transform the 440 landmarks and semi-landmarks of the reference template into the corresponding landmarks and semi-landmarks of M1K12:3, and to warp the surface of the reference template into the area of the target such that the relative transformation required the least possible bending energy. We conducted this process separately for the *Nomascus* and *Hylobates* reference specimens, resulting in two individual reconstructions of M1K12:3 (Fig. S2).

Comparative dataset and landmark data

The comparative dataset used to investigate the cranial morphological affinities of M1K12:3 comes from data collected by ref. 12, the largest available dataset of hylobatid three-dimensional cranial measurements. This dataset consists of 34 three-dimensional anatomical landmarks (Fig. S1) distributed across the cranial surface of 477 hylobatid crania, representing all four extant genera and nearly all extant species: *Hoolock* (*H. hoolock*, *H. leucogenys*, *H. tianxing*), n=53; *Hylobates* (*H. agilis*, *H. albibarbis*, *H. klossii*, *H. lar*, *H. moloch*, "*H. muelleri*" [combined sample of *H. abbotti*, *H. funereus* and/or *H. muelleri*], *H. pileatus*), n=327; *Nomascus* (*N. annamensis*, *N. concolor*, *H. gabriellae*, *N. leucogenys*, *N. siki*), n=34; *Symphalangus* (*S. syndactylus*), n=63 (nomenclature adjusted to reflect currently accepted hylobatid taxonomy; *4*). It is therefore sufficiently

extensive and diverse to be representative of the extent of cranial morphological variation between extant hylobatids.

We employed landmark-based geometric morphometric techniques (*30*) to analyze cranial shape variation. Of the 34 landmarks available in the comparative dataset, it was possible to place 16 (orbitale interior, zygoorbitale, zygomaxillare, nasomaxillare, nasale, nasospinale, prosthion, postmolare II, bregma, glabella, nasion, nasomaxillary suture, orbitale superior, frontomalare orbitale, stephanion, frontomalare temporale) on the surface of the completed reference-based reconstructions (Fig. S1). All other landmarks were omitted either because they occupied areas not able to be reconstructed, or because precise landmark location on existing morphology was ambiguous due to damage or difficulty extracting surface detail from scan data. We then digitized three-dimensional landmark points on the reconstructions of M1K12:3 using Landmark software version 3.0.0.6 (*31*).

Statistical analyses

We used the software package MorphoJ (*32*) to conduct all geometric morphometric analyses of landmark data. We investigated two different datasets of varying landmark number. First, we analyzed all 34 landmarks without including the reconstructions of M1K12:3, to establish the extent of overall cranial shape variation between the four extant hylobatid genera and determine whether distinct morphotypes can be identified using these data. We then conducted a separate analysis using only the reduced set of 16 landmarks and including the compatible reconstructions of M1K12:3, to assess the morphological affinities of this specimen to extant hylobatids.

We performed Procrustes analysis to eliminate all non-shape elements of variation in the dataset (scaling, rotation and translation), and prepare landmark data to be in the

right format for statistical analysis. We then conducted Principal Component Analysis (PCA) and Canonical Variate Analysis (CVA) of all 34 landmark shape coordinates, and conducted permutation tests (10,000 random permutation rounds) to test for significant shape differences between genera. PCA was unable to differentiate between extant hylobatid genera (results not shown), and so only CVA was used in subsequent analyses.

We then conducted CVA and permutation tests for the reduced dataset containing 16 landmarks and M1K12:3, both to explore how successfully the reduced landmark number was able to replicate results from the 34-landmark analysis, and also to determine the morphological and taxonomic affinities of M1K12:3 to the comparative hylobatid dataset. The two separate reconstructions of M1K12:3 were analysed together in cranial shape analyses as a combined "population" of two samples; each reconstruction was also analysed on its own against the comparative hylobatid dataset using the reduced 16-landmark analysis, with no difference in results (results not shown).

3. MOLAR DATA

Comparative dataset

The comparative molar sample comprises a total of 279 individuals (789 M1-3, m1-2 teeth) representing all four extant hylobatid genera (Table S4). We collected data from skeletal collections in the following institutions: American Museum of Natural History, New York (AMNH); Institute of Zoology, Chinese Academy of Sciences, Beijing (IOZ); Kunming Institute of Zoology, Chinese Academy of Sciences, Kunming (KIZ); Museum of Comparative Zoology, Cambridge, Massachusetts (MCZ); Natural History Museum,

London (NHM); South China Institute of Endangered Animals, Guangzhou (SCIEA); National Museum of Natural History, Washington, D.C. (USNM); Zoological Museum, Vietnam National University, Hanoi (ZMVNU). We obtained provenance information from museum records, and nomenclature was again adjusted to reflect currently accepted hylobatid taxonomy (*4*). No antimeres were included. We also included the m2 of the holotype of *Bunopithecus sericus* (AMNH-18534; with no known paratypes; *10*).

Data for different specimens were collected using either digital photographs or a NextEngine 3D Laser Scanner. There are no significant differences in molar crown area between data derived from digital photographs and from screenshots of the 3D surface models, in specimens for which both datasets are available (t = -0.457, df = 18, p = 0.653).

Data acquisition and statistical analyses

We conducted all analyses on high-resolution images of the occlusal surface of teeth taken with either a Canon Digital Rebel XT camera with a 75-300 mm lens (for skeletal material) or Amira imaging software (FEI; for laser scans). We oriented each tooth independently following well-known protocols described elsewhere (*10*, *33*–*35*). We imported digital images of the upper and lower molars into Adobe Photoshop® to align the longitudinal groove with the y-axis and the main buccolingual groove with the x-axis. We mirror-imaged right teeth to correspond to the left side, and treated them as such for landmark digitizing and analyses.

Although cusp areas were successfully used in a previous analysis of the dental affinities of *Bunopithecus* to extant hylobatids, we could not use the same set of variables in this study, as most fissures separating the molar cusps of the teeth of M1K12:3 are obliterated by wear or damage. Instead, we collected morphometric data

on crown outline, cusp angles, and crown and polygon areas of these teeth. We placed homologous landmarks at the cusp tips of the four (upper molars) or five (lower molars) main cusps using tpsDig 232 (*36*) (Figs S3-S4). We used these landmarks to calculate the cusp angles formed by the lines connecting the apices of three given adjacent cusps, which were only digitized on unworn or minimally worn teeth (up to wear stage 3 of ref. 37). Similarly, we calculated polygon area as a ratio of the area enclosed by the four (upper molars) or five (lower molars) main cusps relative to the overall crown size. Finally, we collected the crown outline of each tooth in tpsDig 232 (*36*), which allows the automatic placement of coordinates along the 2D contour of an object, using 20 and 22 equidistant semi-landmarks on the upper and lower molars, respectively (Figs S3-S4). We also collected crown area measurements in Adobe Photoshop® from photographs of those teeth in which a millimetre scale was originally added. All occlusal photographs/screenshots and landmarks and area measurements were collected by AO.

We then conducted multivariate analyses on crown outline data. We were unable to collect outline or polygon area for the M1 of M1K12:3 due to damage on its distolingual portion, and could only use data for angles associated with protocone, paracone and metacone of this tooth. We transformed semi-landmarks using a Generalized Procrustes Analysis to remove differences in size and orientation between individuals, conducted PCAs, and used the principal component coordinates to calculate Mahalanobis and Procrustes distances. We also conducted CVAs to determine generic differences between hylobatids and the molar shape affinities of M1K12:3. We quantified accuracy of CVAs by determining the percent of individuals correctly classified. We conducted all analyses in MorphoJ (*32*) and PAST (*38*).

Supporting Online Material: Systematic paleontology

Order Primates Linnaeus 1758

Suborder Haplorhini Pocock 1918

Parvorder Catarrhini Geoffroy 1812

Superfamily Hominoidea Gray 1825

Family Hylobatidae Gray 1870

Remarks: The skull, mandible and dentition of M1K12:3 exhibit a series of key diagnostic characteristics of the Hylobatidae (*39, 40*), including: a small, shallow face with a modest brow ridge; large orbits with protruding rims which are relatively larger than found in the rest of the Hominoidea; a shallow, gracile mandible; long canines with relatively large proximal bucco-lingual width, tapering to a narrow distal point, and with a distinct mesial sectorial ridge running the length of the tooth; low-crowned, relatively simple molars with low and rounded cusps, with a subrectangular crown outline and rounded corners, and with a simple fissure pattern with minimal and poorly defined crests and no secondary wrinkling; upper molars with four cusps, lower molars with five cusps.

Genus *Junzi* gen. nov.

Type species: *Junzi imperialis* gen. et sp. nov.

Etymology: *Junzi*, from the pinyin (standard mainland Chinese phonetic alphabet) transliteration of 君子, meaning "scholarly gentleman" or "man of virtue or noble character". Gibbons were widely regarded as a symbol of scholar-officials or *junzi* in

ancient China, as the perceived “noble” characteristics of gibbons were considered to accord with the aesthetic taste of both Daoism and traditional Chinese scholars (*7*, *41*).

Diagnosis: *Junzi* differs from extant and extinct hylobatid genera according to the following characters:

Compared to *Hoolock*, has a steeper frontal region; a more superior nasal bone; an inferior expansion along the lower margin of the nasal aperture; a smaller metaconid angle on m1; a smaller protoconid angle on m2; an entoconid facing the protoconid on m1 and m2; and a more inferior position of m2.

Compared to *Hylobates*, has a steeper frontal region; a more superior nasal bone; an inferior expansion along the lower margin of the nasal aperture, which also protrudes further forward posteriorly together with the position of the prosthion; a larger total occlusal area on M2, M3 and m2; no evidence of M3 reduction; a smaller metaconid angle on m2; a more inferior position of m2; and lacks accessory cusps and crests (e.g. mesial marginal accessory cusps,crista/cristid oblique) in post-canine teeth.

Compared to *Nomascus*, has a steeper frontal region; a more superior nasal bone; an inferior expansion along the lower margin of the nasal aperture, which also protrudes further forward posteriorly; a larger paracone angle on M3; a smaller protoconid angle on m1; a smaller metaconid angle on m2; an entoconid facing the protoconid on m1 and m2; a more inferior position of m2; and lacks well-developed cingular structures in post-canine teeth except for M3, which shows a well-developed lingual cingulum.

Compared to *Symphalangus*, has a steeper frontal region; an enlarged orbit characterized by a lateral and inferior shift; a flatter and smaller nasal bone; a more superior prosthion; a more antero-inferior position of m2; an overall shorter alveolar rim; a smaller total occlusal area on M1, m1 and m2; a smaller protoconid angle on m1;

a smaller entoconid angle on m2; an entoconid facing the protoconid on m1 and m2; and lacks vertical wrinkles on the lingual surface of the protocone.

Compared to *Bunopithecus*, has larger lower molars as a result of distal molar expansion associated with expansion of the talonid (such that the overall area of the talonid is larger than that of the trigonid, rather than having a trigonid larger than the talonid as in *Bunopithecus*), and has a smaller buccolingual mesial/distal molar ratio; and m2 rather than m3 is the biggest tooth in the molar row.

Description: The face is small and shallow, and the frontal, nasal and maxilla are not prognathic compared to Old World monkeys of a similar size. The frontal is gracile with a small indistinct brow ridge; steeply oriented; descending to a narrow nasal aperture with a short nasoalveolar clivus. The maxilla protrudes anteriorly to accommodate enlarged canine roots; infraorbital foramina are present, parallel in position with the upper canines. The frontozygomatic suture is positioned anteriorly. The orbits are relatively large and subcircular, with distinctive orbital rims. The mandible is shallow and gracile, narrow anteriorly with an elongated posterior palatal width. The mandibular body is relatively robust with no mental protuberance, and the mental foramen is parallel with the canines and p3.

The dental formula is 2.1.2.3. The incisors are relatively small and spatulate, with a concave lingual surface. The upper and lower canines are relatively large, such that canine size is at the upper end of the range of variation of extant hylobatids; with relatively large proximal bucco-lingual width, tapering to a narrow distal point, and with a distinct mesial sectorial ridge running their length. Upper premolars possess two main low and rounded cusps, the paracone and protocone; the protocone is less elevated than the paracone. P4 is slightly larger than P3 due to presence of a small and low tubercle on the distolingual portion of the tooth crown, and a barely discernible

distobuccal tubercle at least on the left P4. Mesiodistally, greatest length of P3 is on its buccal portion, and greatest length of P4 is on its lingual portion. The p4 is trapezoidal-shaped due to the presence of a very well-developed entoconid. Overall, p4 shape resembles that of *Hoolock hoolock* from Myanmar (*5*), and differs from the oval or round configuration more commonly seen in other hylobatids.

The molars are relatively simple, with low conical cusps and no accessory cusps or crests. The upper molars show the standard hominoid crown configuration, with a subrectangular outline and four low and rounded cusps. A crista obliqua connecting the paracone and metacone is absent or poorly defined. The lingual cusps are less elevated than their buccal counterparts, although this feature is less marked in M3. The hypocone in M1 is relatively small. The protocone is the most well-developed cusp, followed by the metacone. In contrast, the hypocone in M2 and M3 is well-developed, and in M2 is only marginally smaller than the protocone, with all cusps being approximately equal in size. M3 exhibits a small cusp 5 and possibly also a cusp 6 on the distal portion of the tooth. The lower molars also possess a subrectangular crown configuration with well-rounded corners and low cusps, exhibiting the standard hominoid five cusps with a Y-shaped fissure pattern. The crown outline flares slightly distally, so that the talonid is broader than the trigonid. The lingual cusps are slightly more elevated than both the protoconid and the hypoconid. The metaconid is the largest cusp in both m1 and m2. No accessory cusps are present. The entoconid faces the protoconid on m1 and m2. The hypoconulid is centrally located.

Molar proportions show a unique pattern, in which M2 is only marginally larger than M3, and M1 is considerably smaller; extant hylobatids tend to have M1 and M3 that are subequal in size, with M2 being considerably larger. There is no evidence of M3 reduction. Molars also possesses smaller polygon areas relatively to crown size,

suggesting that the cusps are more externally placed than in extant hylobatids. Linear measurements for both upper and lower molars are only slightly larger mesiodistally than buccolingually, with length-breadth indices as follows: M1, 0.98; M2, 1.02; M3, 0.91; m1, 1.10; m2, 1.32. The angle of the paracone is the largest cusp angle in all upper molars, in contrast to all extant hylobatids, and the protocone has a relatively small angle. The angle of the metacone is the largest angle in M2, and the smallest angle in M3. The angles of the protoconid and metaconid are the smallest angles in both m1 and m2, while the angle of the entoconid in m2 is on average the largest for all hylobatid teeth examined.

***Junzi imperialis* gen. et sp. nov.**

Holotype: Shenheyuan M1K12:3 (Fig. 1), comprising a partial facial skeleton missing the posterior neurocranium, with complete anterior dentition, left and right PM3-4 and right M1-2; an associated right M3; and a partial mandible with almost complete anterior dentition (missing left I2), left and right pm3-4 and right m1-2; and right distal forelimb elements.

Etymology: Referring to the discovery of the holotype in a Warring States period imperial or high-status tomb (possibly the tomb of Lady Xia).

Common name: Lady Xia's gibbon or Imperial gibbon.

Type locality: Northwest Shenheyuan plateau (north of the Yu River), Chang'an District, Xi'an Municipality, southern Shaanxi Province, China.

Age: Site not directly dated, but probably from late Warring States period of Zhou Dynasty (*c.*2,200–2,300 BP).

Diagnosis: As for genus.

Description: Morphological description as for genus. Measurements of holotype as follows:

Cranium: I1 buccolingual diameter = 3.94 mm; I1 mesiodistal diameter = 4.91 mm; I2 buccolingual diameter = 4.27 mm; I2 mesiodistal diameter = 4.05 mm; C1 buccolingual diameter = 6.37 mm; C1 mesiodistal diameter = 9.70 mm; C1 labial height = 22.16 mm; P3 buccolingual diameter = 6.29 mm; P3 mesiodistal diameter = 5.26 mm; P4 buccolingual diameter = 6.90 mm; P4 mesiodistal diameter = 5.37 mm; M1 buccolingual diameter = 7.17 mm; M1 mesiodistal diameter = 7.02 mm; M2 buccolingual diameter = 7.81 mm; M2 mesiodistal diameter = 7.98 mm; M3 buccolingual diameter = 7.78 mm; M3 mesiodistal diameter = 7.05 mm; interorbital breadth = 10.31 mm; nasion-nasospinale = 33.22 mm; maximum nasal width = 14.19 mm; canine interalveolar distance = 19.06 mm; palate depth at M1 = 10.88 mm.

Mandible: p3 buccolingual diameter = 8.08 mm; p3 mesiodistal diameter = 4.85 mm; p4 buccolingual diameter = 5.02 mm; p4 mesiodistal diameter = 6.63 mm; m1 buccolingual diameter = 5.85 mm; m1 mesiodistal diameter = 6.45 mm; m2 buccolingual diameter = 6.43 mm; m2 mesiodistal diameter = 8.48 mm; symphyseal height = 21.40 mm; distance between left and right symphyseal fossae = 19.80 mm.

Additional upper and lower molar measurements are given in Tables S6-S7.

The following taxonomically non-diagnostic right distal forelimb elements are also preserved: distal fragment of radius (maximum length = 143.37 mm); distal fragment of ulna (maximum length = 71.77 mm); seven carpals; three metacarpals (largest is the 3rd or 4th right metacarpal; maximum length = 76.53 mm); and four phalanges (1st midline phalange, maximum length = 58.33 mm; 2nd midline phalange, maximum length = 55.56 mm; broken phalange, maximum preserved length = 35.07 mm; small phalange, maximum length = 23.75 mm).

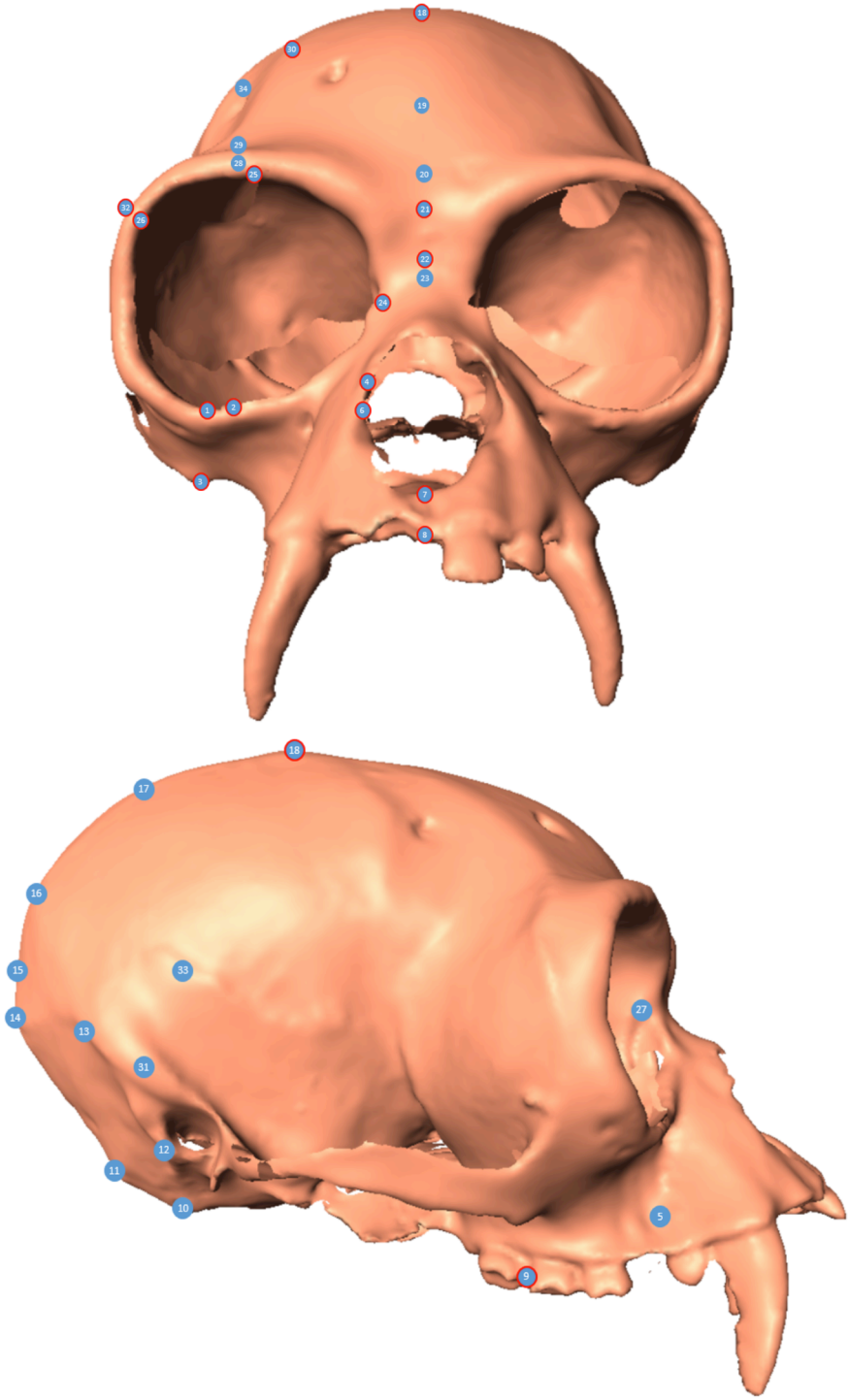

Figure S1. Gibbon cranial landmarks available in Creel and Preuschoft (1976); landmarks used in this study for comparative analysis indicated in red. 1, orbitale inferior; 2, zygoorbitale; 3, zygomaxillare; 4, nasomaxillare; 5, maxillary incision; 6, nasale; 7, nasospinale; 8, prosthion; 9, postmolare II; 10, basion; 11, opisthion; 12, mastoidale; 13, asterion; 14, inion; 15, opisthocranion; 16, lambda; 17, lambda-bregma apex; 18, bregma; 19, bregma-nasion apex; 20, supraglabella; 21, glabella; 22, nasion; 23, nasal roof; 24, nasomaxillary suture; 25, orbitale superior; 26, frontmalare orbitale; 27, maxillofrontale; 28, torion; 29, supratorion; 30, stephanion; 31, supramastoidal crest; 32, frontomalare temporale; 33, euryon; 34, parietal vault elevation.

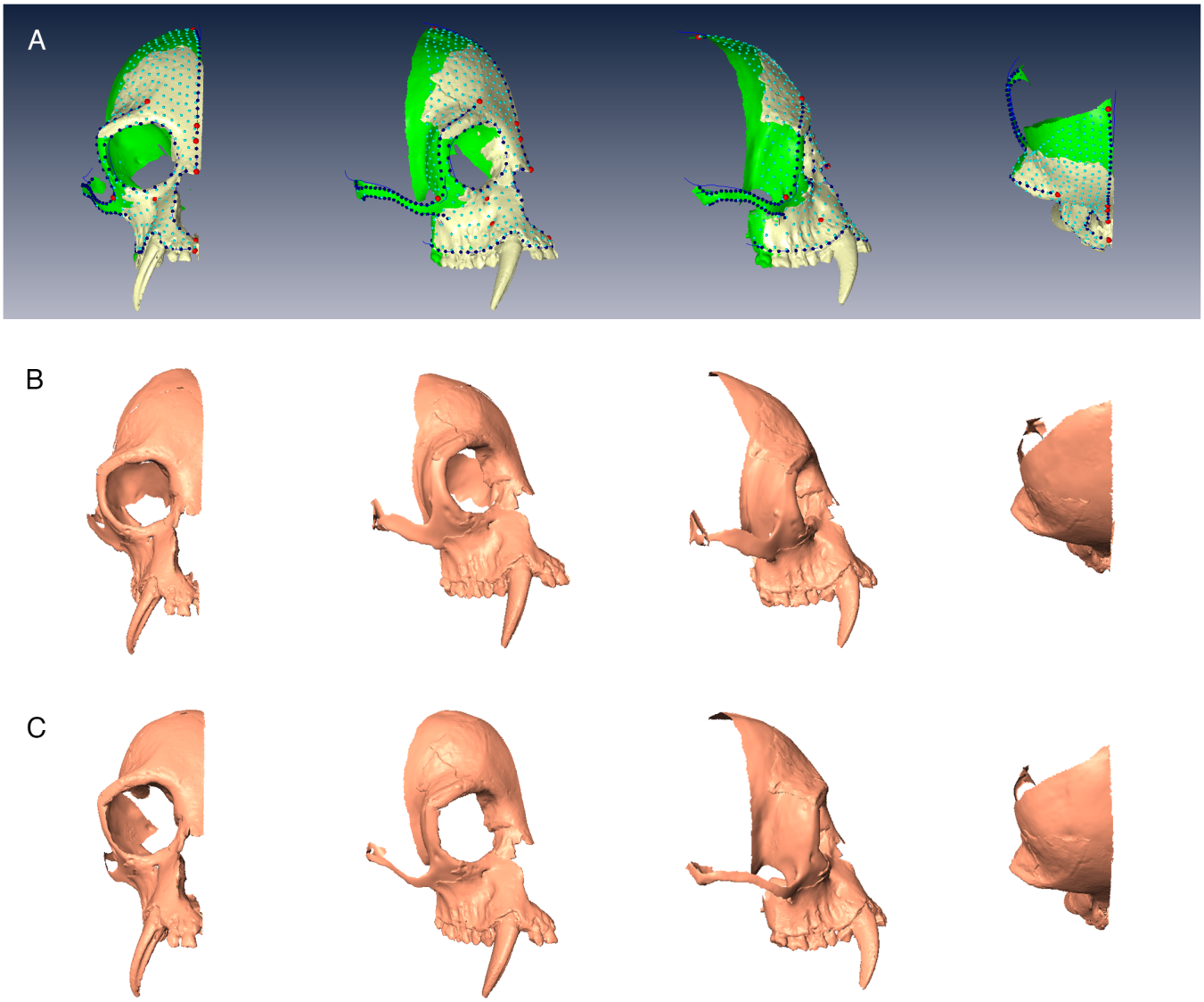

Figure S2. Reference-based reconstruction of M1K12:3. **A**, Reconstructing M1K12:3 using *Nomascus concolor* reference cranium, showing three-dimensional visualisation of M1K12:3 cranium (partially restored through mirror-imaging) in pale yellow, reconstructed areas in green, landmarks in red, curve semi-landmarks in dark blue, and surface semi-landmarks in light blue. **B**, Partially restored cranium of M1K12:3 based on *Hylobates lar* reference cranium. **C**, Partially restored cranium of M1K12:3 based on *Nomascus concolor* reference cranium.

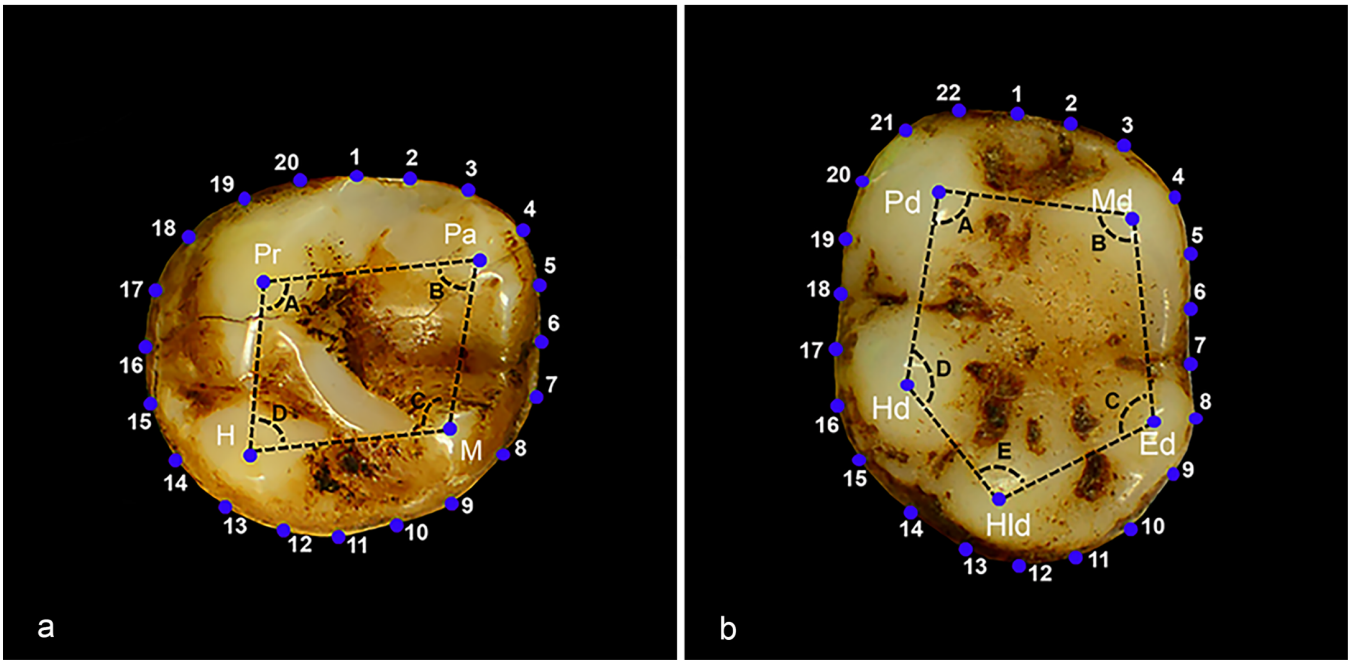

Figure S3. Landmarks and semi-landmarks used in comparative analysis of upper and lower molars. **a**, Upper molars: Pr, protocone (angle A); Pa, paracone (angle B); M, metacone (angle C); H, hypocone (angle D). **b**, Lower molars: Pd, protoconid (angle A); Md, metaconid (angle B); Ed, entoconid (angle C); Hd, hypoconid (angle D); Hld, hypoconulid (angle E).

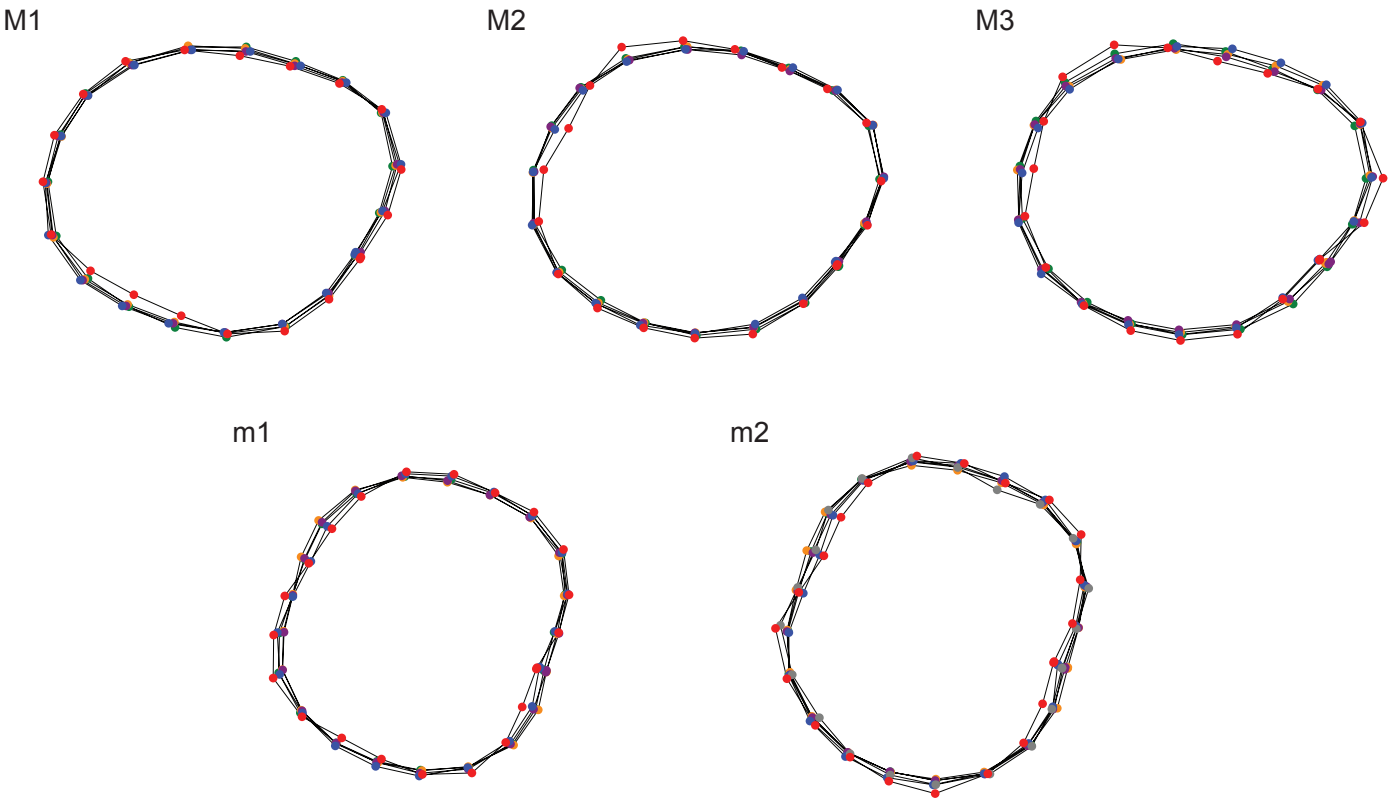

Figure S4. Comparisons of molar crown variation between M1K12:3, *Bunopithecus*, and extant hylobatids based on mean shape outlines. Outlines are of left molars; for M1-M3 the lingual surface is located to the left, and for m1-m2 the lingual surface is located to the right in each image. Key: M1K12:3, red; *Bunopithecus*, gray (m2 only); *Hoolock*, green; *Hylobates*, orange; *Nomascus*, purple; *Symphalangus*, blue.

Table S2. Variance and eigenvalues for cranial and molar CVAs. Data for first three axes provided.

CVA results	Cranium	M1	M2	M3	m1	m2
Axis 1, % variance	60.90	36.58	46.77	43.33	43.67	41.89
Axis 1, Eigenvalue	4.92	1.35	1.11	1.80	2.04	1.85
Axis 2, % variance	23.03	32.19	21.70	29.03	29.37	24.83
Axis 2, Eigenvalue	1.86	1.19	0.51	1.21	1.37	1.09
Axis 3, % variance	10.44	21.26	20.44	16.78	15.82	17.92
Axis 3, Eigenvalue	0.84	0.79	0.48	0.70	0.74	0.79

Table S3. Cross-validation results for cranial and molar CVAs. Main value = not jackknifed; value in parentheses = jackknifed.

A. Cranium							
	Hoolock	*Hylobates*	*Nomascus*	*Junzi*	*Symphalangus*	Total	
Hoolock	52 (50)	1 (3)	0 (0)	0 (0)	0 (0)	53	**Not jackknifed:** 97.5% correctly classified
Hylobates	3 (5)	319 (314)	5 (8)	0 (0)	0 (0)	327	
Nomascus	0 (0)	0 (0)	34 (34)	0 (0)	0 (0)	34	
Junzi	0 (0)	0 (0)	0 (0)	2 (2)	0 (0)	2	
Symphalangus	3 (3)	0 (0)	0 (0)	0 (0)	60 (60)	63	**Jackknifed:** 96.0% correctly classified
Total	58 (58)	320 (317)	39 (42)	2 (2)	60 (60)	479	
B. M1							
	Hylobates	*Symphalangus*	*Hoolock*	*Nomascus*	*Junzi*	Total	
Hylobates	58 (42)	0 (3)	6 (10)	1 (8)	0 (2)	65	**Not jackknifed:** 86.3% correctly classified
Symphalangus	1 (1)	9 (6)	0 (3)	1 (1)	0 (0)	11	
Hoolock	3 (7)	1 (2)	35 (28)	2 (4)	0 (0)	41	
Nomascus	4 (10)	0 (1)	1 (4)	23 (13)	0 (0)	28	
Junzi	0 (1)	0 (0)	0 (0)	0 (0)	1 (0)	1	**Jackknifed:** 61.0% correctly classified
Total	66 (61)	10 (12)	42 (45)	27 (26)	1 (2)	146	
C. M2							
	Hylobates	*Symphalangus*	*Hoolock*	*Nomascus*	*Junzi*	Total	
Hylobates	72 (53)	5 (9)	14 (23)	7 (12)	0 (1)	98	**Not jackknifed:** 76.3% correctly classified
Symphalangus	0 (3)	15 (10)	3 (4)	0 (1)	0 (0)	18	
Hoolock	5 (11)	5 (7)	41 (27)	0 (5)	0 (1)	51	
Nomascus	6 (7)	0 (2)	2 (4)	22 (17)	0 (0)	30	
Junzi	0 (0)	0 (0)	0 (0)	0 (0)	1 (1)	1	**Jackknifed:** 54.6% correctly classified
Total	83 (74)	25 (28)	60 (58)	29 (35)	1 (3)	198	
D. M3							
	Symphalangus	*Hylobates*	*Hoolock*	*Nomascus*	*Junzi*	Total	
Symphalangus	12 (7)	0 (2)	0 (1)	0 (2)	0 (0)	12	**Not jackknifed:** 80.7% correctly classified
Hylobates	1 (7)	53 (42)	12 (16)	3 (4)	0 (0)	69	
Hoolock	0 (0)	3 (6)	27 (20)	1 (5)	0 (0)	31	
Nomascus	3 (3)	2 (4)	2 (6)	20 (14)	0 (0)	27	
Junzi	0 (0)	0 (0)	0 (0)	0 (1)	1 (0)	1	**Jackknifed:** 59.3% correctly classified
Total	16 (17)	58 (54)	41 (43)	24 (26)	1 (0)	140	
E. m1							
	Hylobates	*Symphalangus*	*Hoolock*	*Nomascus*	*Junzi*	Total	
Hylobates	49 (37)	2 (6)	8 (13)	3 (6)	0 (0)	62	**Not jackknifed:** 84.4% correctly classified
Symphalangus	0 (3)	10 (2)	0 (3)	0 (2)	0 (0)	10	
Hoolock	3 (7)	0 (2)	27 (17)	0 (4)	0 (0)	30	
Nomascus	2 (6)	0 (3)	1 (3)	16 (6)	0 (1)	19	
Junzi	0 (0)	0 (1)	0 (0)	0 (0)	1 (0)	1	**Jackknifed:** 50.8% correctly classified
Total	54 (53)	12 (14)	36 (36)	19 (18)	1 (1)	122	
F. m2							
	Symphalangus	*Hylobates*	*Hoolock*	*Nomascus*	*Bunopithecus*	*Junzi*	Total
Symphalangus	22 (15)	0 (4)	0 (2)	0 (1)	0 (0)	0 (0)	22
Hylobates	1 (3)	84 (71)	12 (20)	3 (6)	0 (0)	0 (0)	100
Hoolock	0 (1)	2 (10)	39 (26)	3 (6)	0 (1)	0 (0)	44
Nomascus	0 (2)	4 (4)	4 (8)	13 (6)	0 (1)	0 (0)	21
Bunopithecus	0 (0)	0 (0)	0 (1)	0 (0)	1 (0)	0 (0)	1
Junzi	0 (1)	0 (0)	0 (0)	0 (0)	0 (0)	1 (0)	1
Total	23 (22)	90 (89)	55 (57)	19 (19)	1 (2)	1 (0)	189

Not jackknifed: 84.7% correctly classified

Jackknifed: 62.4% correctly classified

Table S5. Significance of comparisons between extant hylobatid genera for permutation tests (10,000 permutation rounds) of molar Procrustes distances. Non-significant differences in red.

	Hoolock	*Hylobates*	*Nomascus*
M1			
Hylobates	0.0006		
Nomascus	<.0001	0.0025	
Symphalangus	<.0001	<.0001	0.0104
M2			
Hylobates	<.0001		
Nomascus	<.0001	0.1698	
Symphalangus	<.0001	0.0901	0.0458
M3			
Hylobates	<.0001		
Nomascus	<.0001	0.0031	
Symphalangus	<.0001	0.0064	<.0001
m1			
Hylobates	<.0001		
Nomascus	0.0422	0.0678	
Symphalangus	0.0079	<.0001	0.0346
m2			
Hylobates	<.0001		
Nomascus	0.2157	0.0006	
Symphalangus	<.0001	<.0001	0.0001

Table S6. Linear dimensions of upper and lower molars of *Junzi imperialis* compared with extant hylobatids (in mm). Extant hylobatid data from refs 42-44.

		Junzi imperialis	*Nomascus concolor*	*Nomascus leucogenys*	*Hoolock hoolock*	*Symphalangus syndactylus*	*Hylobates agilis*	*Hylobates lar*	*Hylobates moloch*	*Hylobates klossii*
M1	N	1	8	6	17	36	16	26	11	8
	Mediodistal mean (range)	7.02	6.1 (5.9-6.4)	6.3 (5.9-6.6)	6.7 (6.1-7.2)	7.6 (6.0-8.3)	5.9 (5.5-6.7)	5.7 (5.3-6.2)	5.7 (4.7-6.6)	5.4 (5.0-5.6)
	Buccolingual mean (range)	7.17	6.8 (6.5-7.3)	6.7 (6.2-7.1)	7.0 (6.6-7.7)	7.2 (6.2-8.3)	6.3 (5.7-6.7)	6.2 (5.8-7.0)	6.3 (5.7-6.8)	5.9 (5.4-6.3
M2	N	1	10	10	17	36	17	25	10	8
	Mediodistal mean (range)	7.98	6.7 (5.7-7.2)	6.7 (6.2-7.1)	7.1 (6.7-7.5)	8.1 (6.9-9.0)	6.0 (5.7-6.5)	6.1 (5.2-6.7)	6.3 (5.9-7.3)	5.4 (5.0-5.8)
	Buccolingual mean (range)	7.81	7.1 (6.5-7.7)	7.4 (6.7-7.9)	7.7 (7.0-8.1)	8.0 (6.9-8.8)	6.4 (5.8-6.8)	6.5 (6.1-7.0)	6.5 (5.7-7,2)	5.9 (5.4-6.3)
M3	N	1	7	3	13	26	17	24	9	8
	Mediodistal mean (range)	7.1	6.3 (5.6-6.8)	5.9 (5.2-6.7)	6.4 (5.3-7.0)	7.2 (5-5-8.4)	5.4 (4.9-6.0)	5.3 (4.7-6.2)	5.3 (4.7-5.9)	4.0 (3.3-4.5)
	Buccolingual mean (range)	7.8	7.1 (6.5-7.7)	7.1 (6.4-7.5)	7.3 (6.3-8.1)	7.7 (7.1-9.1)	6.1 (5.2-6.9)	6.1 (5.2-6.8)	6.2 (5.4-7.0)	5.6 (5.4-6.0)
m1	N	1	7	4	16	30	16	25	11	9
	Mediodistal mean (range)	6.45	6.8 (6.5-7.2)	7.1 (6.7-7.5)	6.8 (6.5-7.3)	8.0 (6.9-8.7)	6.3 (5.6-6.8)	6.0 (5.7-6.5)	6.3 (5.7-7.2)	5.9 (5.7-6.1)
	Buccolingual mean (range)	5.85	5.3 (5.0-5.7)	5.4 (5.2-5.7)	5.6 (5.0-6.2)	6.3 (5.4-6.9)	5.2 (5.6-6.8)	5.1 (4.6-5.7)	5.0 4.4-5.8)	4.8 (4.2-5.8)
m2	N	1	9	6	16	30	17	23	10	8
	Mediodistal mean (range)	8.48	7.2 (6.9-7.6)	7.2 (6.3-7.9)	7.6 (7.3-8.5)	8.7 (7.5-9.8)	6.3 (5.9-6.9)	6.2 (5.4-6.6)	6.5 (5.7-7.3)	6.0 (5.5-6.6)
	Buccolingual mean (range)	6.43	5.8 (5.4-6.3)	6.0 (5.5-6.6)	6.6 (5.9-7.5)	6.9 (6.1-7.5)	5.6 (5.2-6.4)	5.4 (4.9-6.0)	5.6 (4.9-6.3)	5.1 (4.8-5.2)

Table S7. Descriptive statistics for molar cusp angles and polygon and occlusal areas in M1K12:3 and extant hylobatid genera.

Features	M1K12:3	*Hoolock*			*Hylobates*			*Nomascus*			*Symphalangus*		
		n	Mean	SD	n	Mean	SD	n	Mean	SD	n	Mean	SD
M1 ANPARA	1.964	26	1.84	0.08	36	1.77	0.16	7	1.79	0.26	5	1.88	0.07
M1 OCCLAREA	33.226	6	39.62	5.85	19	31.84	3.56	24	34.24	3.41	7	**49.62**	**7.84**
M2 APOL	0.336	36	0.36	0.03	73	0.37	0.04	6	0.33	0.02	15	0.34	0.04
M2 ANPROTO	1.307	35	1.33	0.11	69	1.41	0.38	8	1.67	0.78	12	1.31	0.08
M2 ANPARA	1.886	35	1.83	0.09	71	1.82	0.17	8	1.70	0.46	13	1.89	0.09
M2 ANMETA	1.352	36	1.30	0.11	74	1.31	0.16	10	1.33	0.33	13	1.26	0.09
M2 ANHYPO	1.738	33	1.81	0.09	67	1.85	0.26	8	1.77	0.69	13	1.83	0.09
M2 OCCLAREA	44.313	14	44.97	5.83	36	**34.21**	**3.77**	27	40.24	4.07	7	57.82	6.87
M3 APOL	0.330	14	0.36	0.03	18	0.36	0.03	6	0.36	0.04	6	0.39	0.05
M3 ANPROTO	1.086	17	1.70	0.53	34	1.95	0.62	7	1.38	0.19	7	1.65	0.62
M3 ANPARA	2.168	16	1.68	0.47	40	1.81	0.51	8	**1.95**	**0.10**	6	1.93	0.13
M3 ANMETA	1.133	18	1.39	0.31	37	1.59	0.56	9	1.20	0.10	6	1.43	0.46
M3 ANHYPO	1.895	16	1.72	0.37	34	1.93	0.62	7	1.77	0.10	6	1.90	0.53
M3 OCCLAREA	43.373	8	39.26	3.39	28	**26.94**	**4.18**	25	36.01	4.40	9	46.91	6.54
m1 APOL	0.362	21	0.37	0.02	39	0.39	0.04	8	0.37	0.03	5	0.37	0.01
m1 ANPROT	1.416	20	1.52	0.09	47	1.58	0.14	9	**1.64**	**0.04**	5	**1.58**	**0.05**
m1 ANMET	1.322	20	**1.45**	**0.05**	44	1.47	0.15	9	1.37	0.06	5	1.41	0.06
m1 OCCLAREA	31.307	20	32.90	4.21	48	28.36	4.00	19	30.37	3.86	8	**44.70**	**4.18**
m2 APOL	0.355	31	0.36	0.03	85	0.37	0.03	8	0.35	0.02	17	0.35	0.02
m2 ANPROT	1.479	32	**1.62**	**0.06**	89	1.57	0.08	8	1.58	0.06	17	1.60	0.06
m2 ANMET	1.246	32	1.40	0.09	89	**1.47**	**0.08**	9	**1.43**	**0.08**	18	1.34	0.14
m2 ANHYP	1.247	32	1.24	0.08	83	1.28	0.13	8	1.26	0.06	18	1.30	0.14
m2 ANENTO	0.999	31	0.82	0.11	83	0.79	0.11	8	0.85	0.09	18	**0.71**	**0.12**
m2 ANHYPLID	1.312	32	1.22	0.11	82	1.17	0.14	8	1.17	0.09	18	1.32	0.10
m2 OCCLAREA	40.933	29	43.82	3.94	89	**30.94**	**4.23**	21	35.21	5.57	22	**54.62**	**5.45**

ANENTO: angle entoconid: ANHYP: angle hypoconid; ANHYPLID: angle hypoconulid; ANHYPO: angle hypocone; ANMET: angle metaconid; ANMETA: angle metacone; ANPARA: angle paracone; ANPROT: angle protoconid; ANPROTO: angle protocone; APOL: ratio polygon area/crown area; OCCLAREA: total occlusal area in mm^2. Angles in radians. Bold/underlined values indicate significant differences with M1K12:3 based on 95% confidence intervals (±2 SD). *Bunopithecus sericus* M2 OCCLAREA: 39.79 mm^2 (Ortiz et al. 2015).